APPLIED SCIENCES AND ENGINEERING

Compliant and stretchable thermoelectric coils for energy harvesting in miniature flexible devices

Kewang Nan[1]*, Stephen Dongmin Kang[2,3]*†, Kan Li[3]*, Ki Jun Yu[4], Feng Zhu[3,5], Juntong Wang[1]‡, Alison C. Dunn[1], Chaoqun Zhou[1]§, Zhaoqian Xie[3], Matthias T. Agne[3], Heling Wang[3], Haiwen Luan[3], Yihui Zhang[6], Yonggang Huang[3]||, G. Jeffrey Snyder[3]||, John A. Rogers[1,3]||

With accelerating trends in miniaturization of semiconductor devices, techniques for energy harvesting become increasingly important, especially in wearable technologies and sensors for the internet of things. Although thermoelectric systems have many attractive attributes in this context, maintaining large temperature differences across the device terminals and achieving low–thermal impedance interfaces to the surrounding environment become increasingly difficult to achieve as the characteristic dimensions decrease. Here, we propose and demonstrate an architectural solution to this problem, where thin-film active materials integrate into compliant, open three-dimensional (3D) forms. This approach not only enables efficient thermal impedance matching but also multiplies the heat flow through the harvester, thereby increasing the efficiencies for power conversion. Interconnected arrays of 3D thermoelectric coils built using microscale ribbons of monocrystalline silicon as the active material demonstrate these concepts. Quantitative measurements and simulations establish the basic operating principles and the key design features. The results suggest a scalable strategy for deploying hard thermoelectric thin-film materials in harvesters that can integrate effectively with soft materials systems, including those of the human body.

INTRODUCTION

Thermal gradients are ubiquitous; thermoelectric devices provide a means for exploiting these gradients in the generation of electrical power (*1*). Here, differences in temperature between the surrounding environment and the human body or an inanimate object/device (*2*–*4*) could provide small-scale amounts of power for operation of wearable sensors or "internet-of-things" devices. Continued advances in electronic components and circuit designs enable aggressive downscaling of power requirements for such systems; the consequences enhance the practical prospects for thermoelectric and other strategies for energy harvesting (*5*–*7*). As examples, integrated processors (*8*) and radio transmitters (*9*) that operate with power in the subnanowatt range can be driven using energy harvested from ambient light (*8*) and the endocochlear potential (*10*), respectively. Pairing such platforms with sensors that have similar power budgets could enable distributed, continuous, and remote environmental or biochemical monitoring (*11*).

A key challenge in the development of miniaturized thermoelectric harvesters is in matching the thermal impedance of heat exchange with the active material in the natural direction of heat flow, typically oriented out of the plane through the device. Thin films have minimal thermal impedance in this direction due to their small thicknesses such that the temperature drop across this direction is, in practical terms of thermoelectric energy harvesting, negligible. As a result, most reported thermoelectric devices based on thin-film materials use thermal gradients that form in the plane (*12*–*14*). In geometries of practical significance, the impedance is rarely matched.

The use of thick films (tens to hundreds of micrometers) deposited by electroplating (*15*, *16*) or printing (*2*, *17*) can help match the out-of-plane thermal impedance, but this approach typically results in harvesters that are rather bulky (*18*). In addition, the heat exchange capabilities from natural air convection in such devices are limited by their planar surface areas. The result could be diminishing output voltage over time as the device reaches a steady-state temperature distribution. Strategies that exploit thin-film materials rolled into cylinders yielding multilayer stacks aligned with thermal gradients in the in-plane direction of the films (*19*) can enhance impedance matching. Parasitic flow of heat through the substrate, which is also aligned with the thermal gradient, represents a design challenge inherent in this approach.

Mechanical compliance is an additional consideration for integrating harvesters with the curved surfaces of the human body or with nonplanar substrates that can be common in internet-of-things applications. Combining thin polymer substrates or metal foils with inorganic thermoelectric films, wires, or ribbons (*2*, *13*, *17*, *20*) represents a well-developed route to flexible systems. Alternative approaches use organic thermoelectric materials or composites (*21*–*30*). In both cases, however, the resulting planar and thin device designs suffer from the challenges in thermal design mentioned above.

Here, we propose and demonstrate an architectural solution to this challenge, in which two-dimensional (2D) device structures formed using planar transfer, deposition, and patterning techniques serve as precursors in the assembly of interconnected arrays of functional, 3D helical coils. In this way, the in-plane direction of thin-film active materials rotates to align toward the out-of-plane direction of the device. This design strategy has the advantage that it is compatible with the most advanced materials and techniques in planar microsystem technologies. In addition, the naturally compliant nature of the coils allows these systems to conform to complex curvilinear surfaces, even those that are time dynamic, thereby ensuring excellent thermal contact with the heat source. Above all, the 3D nature of the system provides a multifold increase of the surface area, resulting in higher overall heat exchange capability and thus higher maximum power.

[1]University of Illinois at Urbana-Champaign, Urbana, IL 61801, USA. [2]California Institute of Technology, Pasadena, CA 91125, USA. [3]Northwestern University, Evanston, IL 60208, USA. [4]Yonsei University, Seoul 03722, Republic of Korea. [5]Wuhan University of Technology, Wuhan 430070, China. [6]Tsinghua University, Beijing 100084, China.
*These authors contributed equally to this work.
†Present address: Stanford University, Palo Alto, CA 94305, USA.
‡Present address: University of Michigan, Ann Arbor, MI 48109, USA.
§Present address: Columbia University, New York, NY 10027, USA.
||Corresponding author. Email: y-huang@northwestern.edu (Y.H.); jeff.snyder@northwestern.edu (G.J.S.); jrogers@northwestern.edu (J.A.R.)

RESULTS

Design and assembly approaches

Our demonstration of this thermoelectric helical coil architecture uses monocrystalline silicon as the active material, as shown in the schematic illustration of Fig. 1A. Here, a mechanically guided assembly (*31*–*35*) generates 3D helical structures from 2D serpentines via compressive buckling induced by relaxing a previously stretched elastomer substrate to which the serpentines bond at selected locations; strong chemical bonds follow from condensation reactions between surface hydroxyl groups on the surface of the elastomer and patterns of silicon oxide (fabrication procedure in fig. S1 and note S1) formed on the serpentines. The serpentines incorporate silicon ribbons with p- and n-type segments, termed p- and n-"legs," connected in a series arrangement by lithographically patterned traces of metal. Polymer coatings formed on the top and bottom sides encapsulate the system (fig. S3) in a manner that also locates the silicon at the neutral mechanical plane to enhance fabrication yields during the bending and twisting deformations associated with transformation from 2D to 3D and during deployment and use. In the final configuration, the legs serve as the pathways for thermal transport between the substrate and the environment. Specifically, as the substrate equilibrates with the thermal source, heat passes into the coils at the bonding locations. The encapsulation layers have widths larger than those of the silicon ribbons to increase the surface area as the cold-side heat exchanger and to provide mechanical support and protection. As mentioned previously, the 3D coils also provide remarkable levels of mechanical compliance and robustness during handling and bending (Fig. 1B), although they incorporate heavily doped silicon (fracture strain ≈ 0.1%) (*36*). The assembly process can naturally scale to large arrays without deviating from the geometry predicted by finite element analysis (FEA) (Fig. 1C). Such characteristics render these systems well suited for forming intimate thermal interfaces to the human body, such as the wrist or ankle (Fig. 1D), as well as other objects with curvilinear shapes. Although the examples presented here use a particular set of materials, fabrication schemes, and device geometries, the overall concepts have broad applicability.

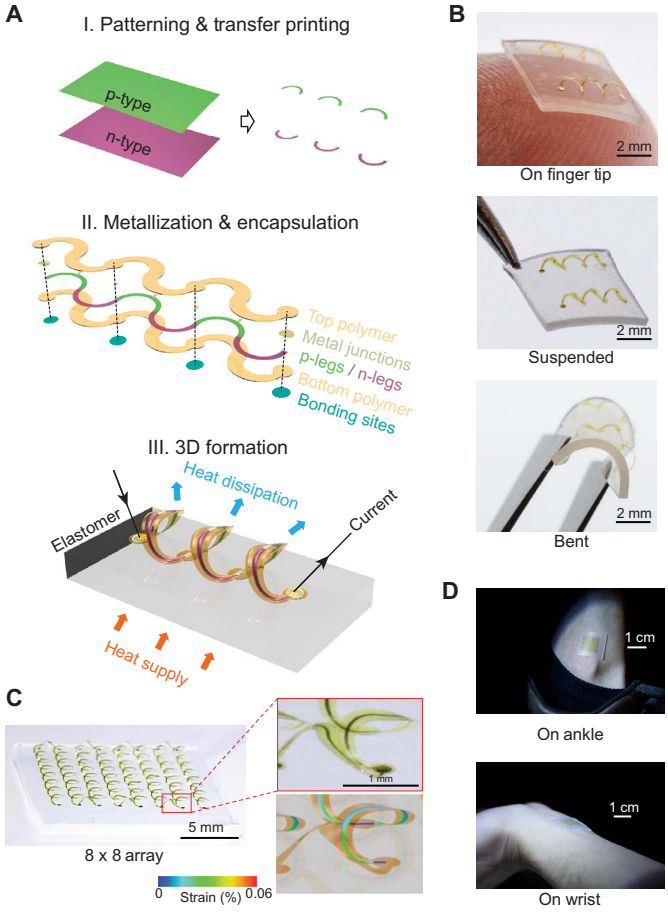

Fig 1. 3D thermoelectric coils as active components of flexible and deformable systems for harvesting electrical power. (**A**) Schematic illustration of the process for fabrication and 3D assembly. Thin-film p- and n-type materials patterned into 2D serpentine shapes and transferred onto a layer of polyimide (PI) define the active materials. Metal junctions and a top coating of PI patterned by photolithography and etching complete the formation of 2D precursor structures. Chemically bonding such systems to a 60% uniaxially prestretched silicone substrate at selective locations (hot-side junctions), followed by release of the prestretch, initiates a process of geometrical transformation that yields the final 3D architectures. See Materials and Methods and the supplementary materials for details. (**B**) Optical images of the resulting 3D thermoelectric coils. The geometry of the structure and the elastomer substrate combine to provide mechanical robustness against handling and mechanical deformation. (**C**) Image of an array with 8 × 8 coils. The magnified view shows that the 3D structure has a geometry consistent with that predicted by FEA. The colored profile represents strain in the silicon leg. The design of the 2D precursor can be found in fig. S2. (**D**) The 8 × 8 array attached to the skin. Photo credit: Xiwei Shan, UIUC Lab.

FEA for geometry optimization

The mechanical and thermal properties of 3D coils can be accurately predicted by FEA such that a full-scale, thermomechanically coupled model can provide critical guidance on selection of materials and geometrical configurations. An optimized layout based on using silicon (thickness = 0.2 μm) and PI (total thickness = 8 μm) as active and encapsulating materials, respectively, incorporates a tapered serpentine geometry. The unit leg length is 1.57 mm with a constant curvature, and the PI widths at the top and bottom of the leg are 0.34 and 0.17 mm, respectively (i.e., ratio is 2). The following sections summarize the thermal and mechanical aspects of this computationally guided optimization process.

Thermal design principles: Heat exchange and impedance matching

The advantages of the 3D architecture follow from a set of thermal aspects that are favorable for effective harvesting, which can be understood with some basic device principles (*1*, *37*). For a total heat flow $\dot{Q}$ [W] through a device, the harvested power can be written as $P = \eta\dot{Q}$, where η is the conversion efficiency. Here, only $\dot{Q}$ through the thermoelectric legs $\dot{Q}_{TE}$, i.e., through silicon in our case, can be converted; any heat bypassing the legs does not contribute to $\dot{Q}_{TE}$ and is referred to as "parasitic." The value of η is proportional to the difference in temperature across the thermoelectric leg ΔT_{TE}, as $\eta \approx \eta_0 \Delta T_{TE}/T_H$, in a harvesting environment that involves small thermal gradients and a given hot-side temperature T_H. Here, η_0 depends on the thermoelectric figure-of-merit (zT) but not on the device design (*1*). According to $P = \frac{\eta_0(zT)}{T_H} \cdot \Delta T_{TE}\dot{Q}_{TE}$, the device design goal with a given thermoelectric material and hot-side temperature is to maximize the product $\Delta T_{TE}\dot{Q}_{TE}$.

Because changes in many geometric parameters of the device (e.g., leg length) change $\dot{Q}_{TE}$ and ΔT_{TE} in opposite directions, the most fundamental limiting factor—the heat exchange capability—should

be optimized at the first step of design. The heat exchange capability describes how well the device can receive and dissipate heat from the hot and cold sources, represented by the inverse of the total thermal impedance for heat exchange $1/\Theta_{ex}$; it determines the upper limit of $\dot{Q}_{TE}$ because $\dot{Q}_{TE} < \Delta T_{Envi}/\Theta_{ex}$, where ΔT_{Envi} is the temperature difference between the heat source and the surrounding environment. Once the design features that give a minimal Θ_{ex} are identified, the next step for optimization is to find specific geometric parameters that could produce the maximum $\dot{Q}_{TE}\Delta T_{TE}$. In traditional device geometries, the optimum point occurs when Θ_{ex} is similar to the impedance of the leg Θ_{TE} (*37*) because Θ_{TE} increases ΔT_{TE} but decreases $\dot{Q}_{TE}$, analogous to load impedance matching in electronics. This condition is the thermal impedance matching condition (note S2). Following this optimization strategy, we first find the design feature that maximizes the heat exchange capability (minimizes Θ_{ex}). We take advantage of the 3D design space that allows a large surface area; in harvesters that rely on passive cooling from air convection, the surface area on the cold side determines the total heat flow. In the 3D helical coil system of Fig. 1, all surfaces except those in contact with the substrate serve as cooling interfaces, with total areas that are much larger than the bonding area. We highlight the role of the leg encapsulation layer, which not only provides mechanical support but also strongly enhances the heat exchange from an enlarged surface area. Analogous to conventional cooling fins, the optimal geometry for cooling is a diverging profile toward the cold side (i.e., top side). We thus use a tapering geometry that increases in width toward the top (Fig. 2). This top-side wide geometry, however, will inevitably increase the load applied to the leg, compromising mechanical stability. Therefore, the thermally favorable design should be limited to within the mechanical stability range.

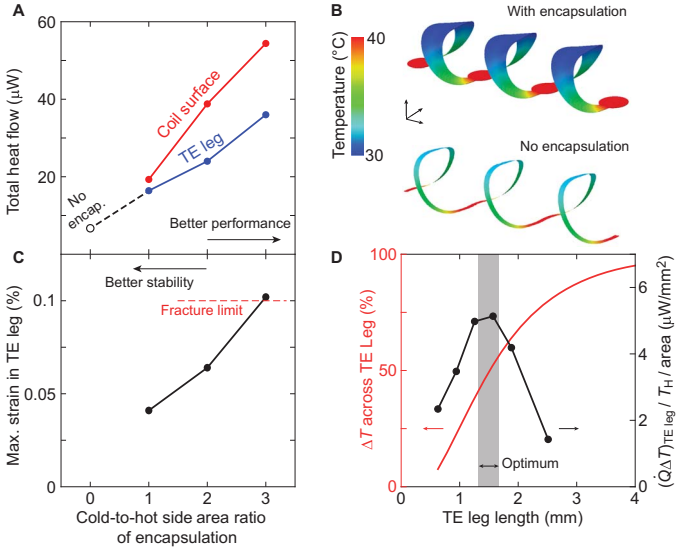

Fig 2. Considerations in thermal engineering to optimize choices of design parameters. (**A**) The total heat flow across the silicon thermoelectric (TE) leg (blue) increases as the width of the cold side of the encapsulated polymer layer is increased. The overall heat dissipation through surface convection (red) increases the heat flow. (**B**) Simulated temperature profiles by FEA that compare the encapsulated case (the ratio of the area of the cold to the hot side is 2) to the non-encapsulated case with identical geometry. The encapsulation lowers the temperature at the cold side of the leg. (**C**) Maximum strain in the thermoelectric leg as a function of the ratio of the area of the cold to the hot side. Increasing the area of the cold side, while desirable for improved performance, compromises the mechanical stability. An area ratio of 2 balances heat exchange capability and mechanical stability. (**D**) With an area ratio of 2, the leg length is selected to maximize $\Delta T_{TE}\dot{Q}_{TE}$ (right axis, normalized to T_H and area), which is the impedance matching condition. The corresponding fractional temperature drop across the leg is shown on the left axis. All findings presented here are the results of modeling of 3 × 1 coil structures (three leg pairs) with a hot-side thermal bath of 40°C and the entire surface subject to convective heat dissipation due to ambient air at 21°C.

To find the optimal tapered geometry, we simulated the dependence of the thermal and mechanical response on the encapsulation layer geometry using FEA. As indicated in Fig. 2A, simply adding a nontapered encapsulation layer to the bare silicon increases $\dot{Q}_{TE}$ by threefold (6.2 to 19.3 μW). Tapering the encapsulation to a higher cold-to-hot side area ratio further increases $\dot{Q}_{TE}$, as expected. The increased heat flow also results in a lower cold-side temperature (Fig. 2B). The maximum strain in the silicon leg also increases with tapering, reaching the silicon fracture limit at a tapered ratio of 3 (Fig. 2C and fig. S4). In addition, the fabrication yield associated with 3D assembly decreases with tapering because buckling in the downward direction (competing with the upward direction) becomes an increasingly favorable mode (note S3 and fig. S5). To remain in the mechanically stable regime, we selected a cold-to-hot side area ratio of 2. We note that this design strategy—to increase the cold-side heat exchange with an encapsulation layer—is unique for 3D thermoelectric harvesters. In an in-plane harvester where the surface area is fixed, substrates and encapsulation layers only increase parasitic heat flow, but not $\dot{Q}_{TE}$.

The next focus is on conditions for thermal impedance matching. High heat flow is only beneficial if thermal impedance matching is possible. This condition can be easily achieved in the 3D coil structure because the leg length can be adjusted up to hundreds or thousands of micrometers; the thermal resistance of the leg is proportional to its length. Simulation results show that the impedance matching condition can be achieved with a leg length of ≈ 1.5 mm (Fig. 2D), at which a maximum in $\Delta T_{TE}\dot{Q}_{TE}$ (normalized by area and T_H) is found. We emphasize that the $\Delta T_{TE}\dot{Q}_{TE}$ calculated here includes only the heat input into the silicon, excluding any parasitic heat. The ability to adjust ΔT_{TE} across such a wide range (and thus obtain the impedance matching condition) in our design is a key differentiating feature relative to conventional film-based harvesters, where only an extremely small ΔT_{TE} is possible in the out-of-plane direction.

We note that our design scheme is optimized for harvesting in miniature devices. Because of the priority on minimal occupied space and weight, cooling is made to rely on natural convection. This cooling process dominates the thermal impedance of the harvester, making other design factors like substrate-to-leg conductance much less important. Instead, increasing the total surface cooling capacity is of utmost priority, exemplified by the fact that the leg encapsulation layer actually enhances the heat flow through the leg (Fig. 2A; 9.7 nW increase in silicon heat flow by adding a nontapered encapsulation) despite the introduction of parasitic heat flow (2.9 nW). That is, the benefit of increased cooling capability greatly outweighs any losses from parasitic heat flow, a regime that might be counterintuitive from the aspect of bulk generators.

Mechanical compliance

One of the key advantages of our device is the mechanical compliance to endure a substantial amount of bending, in-plane stretching, and out-of-plane compression, as opposed to previously reported out-of-plane harvesters (*2*, *15*, *16*, *19*, *20*, *38*) with limited flexibility or stretchability. As shown in Fig. 3, these 3D structures can be stretched in the in-plane direction by up to 60% for hundreds of cycles (Fig. 3, A to C) and can be

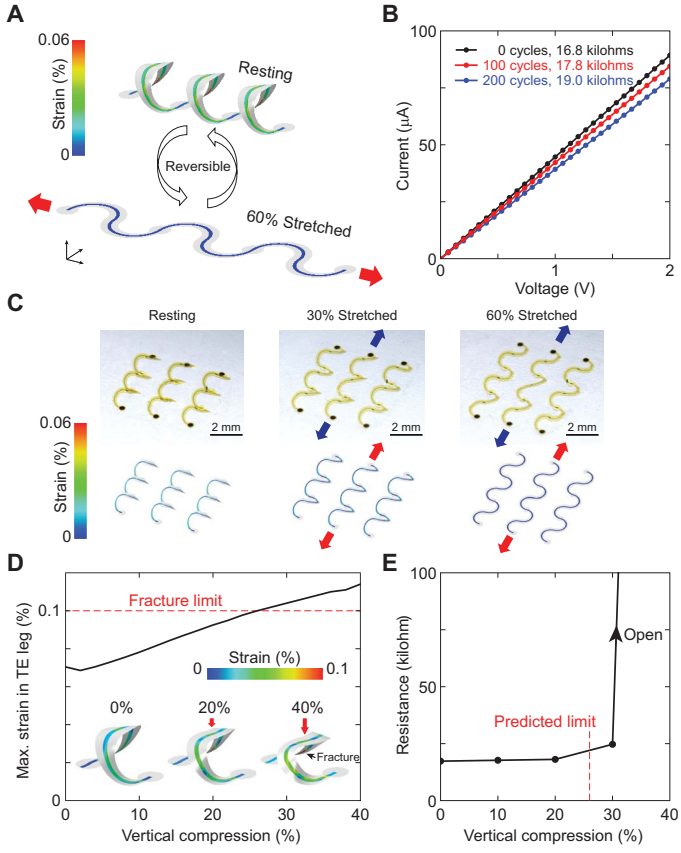

Fig 3. Mechanical deformability and durability of 3D thermoelectric harvesters. (**A**) Simulated distributions of strain in the silicon thermoelectric leg before and after uniaxial stretching in the plane by 60%. The results indicate reductions in strain upon stretching, as expected based on the compressive buckling process used to form the 3D structures. (**B**) Results of experimental durability tests that involve multiple cycles of 60% uniaxial stretch and release on a 3 × 1 coil structure (strain rate ≈ 0.01 s^{-1}). The data indicate only a small increase in the electrical resistance. (**C**) Optical images (top row) and simulated structures (bottom row) upon in-plane stretching. (**D**) Simulated values of the maximum local strain in the thermoelectric leg induced by vertical compression. A maximum compression of 26% is possible before reaching the fracture strain of the silicon, the limiting factor for this system. The inset shows the deformed structure upon compression, including a strain distribution map of the silicon leg. The maximum strain occurs near the hot side, indicated as the fracture point (see also fig. S8). (**E**) Experimental measurements of the device resistance upon vertical compression. The onset of an increase in resistance occurs near the limit predicted by simulation. At a compression of 40%, the device shows open-circuit behavior due to fracture of the silicon.

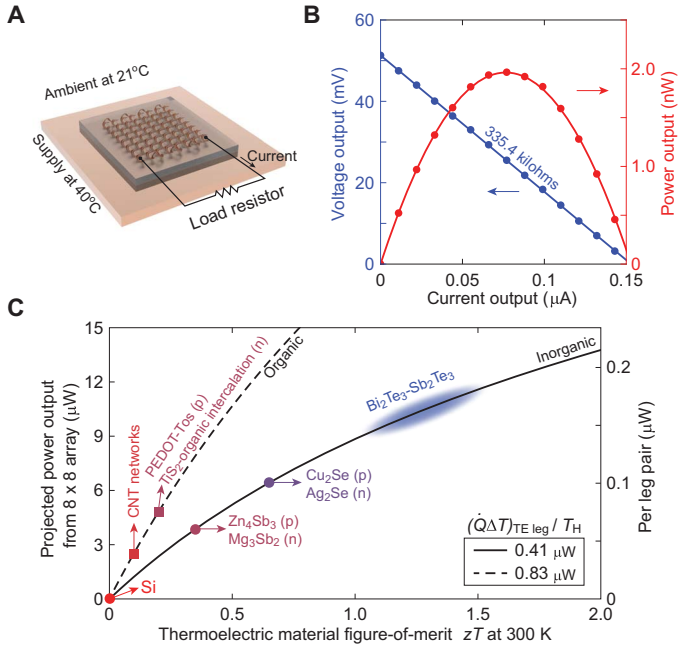

Fig 4. Energy harvesting with thermoelectric coils and a road map for power enhancement. (**A**) Schematic illustration of the measurement conditions for evaluating the performance of the harvesting devices. An 8 × 8 array was exposed to an environmental temperature difference of 19°C. (**B**) Measured power output characteristics of the 8 × 8 coil array, showing a maximum power of 2 nW. (**C**) Projected power output achievable by using known thermoelectric materials with thermoelectric figure-of-merit *zT* higher than that of Si (left axis is for an 8 × 8 array; right axis shows values on a per coil basis). These powers correspond to $\dot{Q}\Delta T/T_H$ per leg values as indicated in the legend and ideal conversion efficiencies. The dashed and solid lines represent the values from structures obtainable with organic and inorganic materials, respectively (see fig. S12). The *zT* values used here correspond to averages of p- and n-type materials reported in the literature: CNT networks (*29*), PEDOT-Tos (*30*), TiS_2-organic intercalation (*21*), Zn_4Sb_3 (*44*), Mg_3Sb_2 (*45*), Cu_2Se (*46*), Ag_2Se (*47*, *48*), and Bi_2Te_3-Sb_2Te_3 (*49*, *50*).

vertically compressed up to 30%, with only minimal degradation in the electric properties (Fig. 3, D and E). This exceptional level of mechanical compliance in a structure that incorporates silicon follows from a design principle that places silicon in the neutral mechanical plane with respect to deformation, as also predicted by FEA. This design also ensures that the strains in the encapsulation and metal layers are well below the threshold for plastic yielding (fig. S6). Stretching in the plane reduces the material strains, as it returns the structure to its original, undeformed 2D geometry. Uniaxial stretching over 200 cycles does not lead to signs of electrical or mechanical failure (Fig. 3, B and C). Comparable results were also found on the 8 × 8 array (Fig. 1C), where 200 cycles of 60% biaxial stretching resulted in a 22% increase in resistance from 335.4 to 409.7 kilohms.

For vertical compression, measurements indicate the onset of changes in resistance at ≈ 30% before fracture of the silicon causes an open circuit (Fig. 3E, fig. S7, and note S4), also consistent with FEA in Fig. 3D and fig. S8. The overall resilience of the 3D coil suggests the potential to interface with various miniature device schemes. For example, suitable designs allow system-level properties that are mechanically and geometrically compatible with those of the soft tissues of the human body.

As most inorganic thermoelectric materials, such as Bi_2Te_3-Sb_2Te_3 alloys (*39*), Zn_4Sb_3 (*40*), and Cu_2Se (*41*), have fracture strains similar to silicon, the measurements and FEA results described above suggest that they could be deployed in similar 3D structures with comparable mechanical properties. The use of thermoelectric materials based on organic polymers could further enhance the mechanics and also the heat flow properties.

Power output and projections

The output characteristics of the harvester (Fig. 4, A and B) that consists of an 8 × 8 array of coils (Fig. 1C) are consistent with the design expectations outlined in previous sections. Using measurement procedures outlined in Materials and Methods and fig. S9, the open-circuit voltage is 51.3 mV at ΔT_{Envi} = 19 K, yielding an estimated temperature drop of

6.2 K across each individual leg based on an average thermopower of 65 μV/K measured from the prepatterned silicon (see fig. S10). This value is consistent with measurements from a 3 × 1 array (6.9 K, fig. S11) and somewhat smaller than the design estimation of 9.5 K (Fig. 2D). The discrepancy follows, at least partly, from uncertainties in the thermal transport parameters used for simulation. In comparison to most literature reports (*2*, *15*), where even bulk material harvesters are operated rather far from thermal impedance matching conditions, these results demonstrate the promise of our matching strategy. The open-circuit voltage does not diminish over time in our measurements, indicating that the thermal profile in our device is at steady state. The maximum power output, i.e., ≈ 2 nW, is modest, mainly due to the low zT of silicon. Some state-of-the-art miniature devices including transmitters or biosensors (*8*–*10*) can be powered at this level, but for current mainstream applications, an improvement in power is required.

The good agreement between modeling and experiment allows the use of simulation results to estimate power outputs for harvesters built with other materials, specifically those with better figure-of-merit $zT > 0.1$ than silicon ($zT > 10^{-3}$ at 300 K). Recall that $P = \eta_0(zT)\cdot\frac{\Delta T_{TE}}{T_H}\dot{Q}_{TE}$. For T_H = 313 K, we simulate $\Delta T_{TE}\dot{Q}_{TE}$ for designs relevant for two different groups of materials, inorganic and organic, while keeping the occupied area of the coil the same as that of the encapsulated silicon design. For organic-based materials (dashed line, Fig. 4C), we find $\Delta T_{TE}\dot{Q}_{TE}/T_H = 0.83\,\mu W$ (similar to the 0.73 μW of encapsulated silicon) based on a design that simply replaces the silicon and encapsulation entirely with the organic thermoelectric material (fig. S12). For inorganic materials (solid line, Fig. 4C), the encapsulation again defines the surface area profile and maintains mechanical stability, but the reduced thermal conductivity compared with silicon results in $\Delta T_{TE}\dot{Q}_{TE}/T_H = 0.41\mu W$ (fig. S12 based on Bi_2Te_3-Sb_2Te_3). Nevertheless, power output is generally higher by virtue of the higher zT, yielding a higher conversion efficiency. Overall, by integrating known thermoelectric materials, the power output at the level of a few microwatts appears to be possible. Such an improvement to 0.15 μW per coil would allow ≈ 100 μW of power from an area of a typical wrist watch (≈ 10 cm^2) when a similar ΔT_{Envi} is given. Room for further improvement up to an order of magnitude in total exists from packing coils more efficiently, using designs better optimized for the low–thermal conductivity thermoelectric material, and stacking the coils in 3D with repeated transfer printing (see fig. S13 for example design) (*42*). Our fabrication scheme is generally compatible with other materials, especially the organic variants in Fig. 4C, which allow minimal use of encapsulation layers.

DISCUSSION

Additional opportunities for improvement in harvesters that use inorganic materials is in the development of thick (or wide) films to reduce the effects of parasitic heat flow through the encapsulation layers while maintaining mechanically stable designs. For organic or composite materials, additional research on methods for deposition, doping, and patterning could yield progress. For all classes of thermoelectric materials, the mechanical properties become more important to understand in the context of the sorts of 3D configurations reported here. A related challenge is to identify materials and compatible metals that do not suffer from electrical resistance increases during the 2D-to-3D mechanical transformation. In the current case of silicon, typically a threefold increase in resistance is observed during the transformation, possibly due to electrode contact degradation and plastic deformation in some parts of the leg. These various areas represent promising directions for future research.

MATERIALS AND METHODS

Patterning and transfer printing of p- and n-doped single-crystalline silicon

Single-crystalline films of silicon with a thickness of 200 nm (silicon-on-insulator, Soitec) served as the thermoelectric material. A layer of SiO_2 (500 nm) formed on the top silicon by plasma-enhanced chemical vapor deposition served as masks for doping. Patterning relied on photolithography and a combination of reactive ion etching (CF_4 + O_2) and wet etching (buffered oxide etchant) to define openings in the SiO_2 for solid-state diffusion doping. The p- and n-type regions resulted from doping with boron (1000°C, 14.5 min) and phosphorus (1000°C, 5.5 min), respectively. Each dopant type required its own SiO_2 mask. A photolithographically patterned layer of photoresist (S1805, MicroChem) defined regions of via holes (3 μm diameter, 50 μm pitch), formed through silicon by reactive ion etching (SF6). These holes also enabled etching of the buried oxide layer by immersing the wafer in 49% hydrofluoric acid for 30 min. Thoroughly rinsing the sample with deionized water prepared it for transfer printing. A flat slab of polydimethylsiloxane (Sylgard 184, 1:4) enabled retrieval of the photoresist/Si film and delivery onto a bilayer of polyamic acid (precursor to form 4-μm PI, PI 2545, HD MicroSystems) and poly(methylmethacrylate) (PMMA; 200 nm, MicroChem) spin coated sequentially on a silicon handling wafer. Immersion in acetone dissolved the photoresist. Baking in a vacuum oven completed the curing of the PI. Last, photolithography and reactive ion etching (SF6) patterned the silicon into isolated p- and n-type serpentine-like layouts.

Fabrication of the 2D thermoelectric precursor and the 3D spring structure

Bilayers of Ti (60 nm)/Au (60 nm) deposited by electron beam evaporation and patterned by photolithography and wet etching served as electrical interconnects between the p- and n-type silicon. This process also defined electrode pads for probing. Spin coating another layer of PI (4 μm) and patterning it by exposure to an oxygen plasma through a mask of photoresist (10 μm, AZ 4620, MicroChem) encapsulated the system and completed the fabrication of the 2D thermoelectric precursor. Dissolving the residual photoresist and the underlying PMMA in acetone allowed the precursor to be retrieved onto a piece of water-soluble tape (Aquasol). A pattern of SiO_x (50 nm) formed by electron beam evaporation through a shadow mask defined bonding sides on the back side of the precursor. An elastomer substrate (Dragon Skin 10, 1:1, Smooth-On Inc.) stretched to the desired level using a stage served as a substrate for 3D assembly. Exposing the elastomer and the 2D precursor (still on a water-soluble tape) to ultraviolet-induced ozone (Jelight UVO-Cleaner, 144AX) and then laminating to the two together and baking them in a convection oven at 70°C formed strong adhesion via condensation reactions at the bonding site interface. Dissolving in warm water removed the tape. Slowly releasing the strain in the elastomer substrate while immersed in water completed the 3D assembly.

Finite element analysis

3D FEA for the thermomechanically coupled system yielded predictions of the mechanical deformations, strain distributions, heat flux, and temperature profiles of the individual 3D coil structures as well as

the arrays (8 × 8 and 3 × 1) during the processes of compressive buckling, restretching, and vertically compressing. Coupled temperature-displacement four-node shell elements with a four-layer (PI/metal/silicon/PI) composite modeled the 3D coil spring. Refined meshes ensured computational accuracy using a commercial software (Abaqus). Parametric designs led to the mechanically and thermally optimized geometric parameters using a commercial software (Isight) coupled with Abaqus. The heat transfer coefficient at the PI surface was set to 5 W/(m^2 · K). The material parameters used were as follows: E_{PI} = 2.5 GPa, ν_{PI} = 0.27, and κ_{PI} = 0.46 W/(m · K); E_{Si} = 130 GPa, ν_{Si} = 0.27, and κ_{Si} = 80 W/(m · K); and E_{metal} = 79 GPa, ν_{metal} = 0.34, and κ_{metal} = 401 W/(m · K). Here, E is the elastic modulus, ν is the Poisson's ratio, and κ is the thermal conductivity.

Thermoelectric characterization

Transport properties of the doped silicon films were characterized at room temperature. Electrical conductivity and Hall measurements used the van der Pauw method with Mo probes. A 2-T electromagnet generated the magnetic field. Measurements of electrical conductivity used an in-line four-point Os probe setup to yield results consistent with those from the van der Pauw method. The in-plane Seebeck coefficient of the doped silicon film was measured using a scanning probe setup (*43*) with a maximum temperature difference of ≈ 8 K. The thermoelectric response of the coil harvester was measured by placing the device on a Cu block that was heated using a film heater attached to the bottom side of the block. A type K thermocouple was attached to the bottom of the harvester substrate, and the film heater was PID controlled to maintain the harvester bottom temperature at 40°C. Room temperature was measured using another type K thermocouple placed in air near the harvester. The entire setup was built inside a probe station enclosed in a dark box. Electrodes were probed using W needles. The output voltage and current were measured at varied load resistances. To achieve the equivalent effect of switching the load resistance, a source measurement unit (Keithley 2400) was used under the current-scanning mode (see also fig. S9).

Mechanical characterization

The cyclic stretching tests involved loading the harvester device onto a stretching stage and then uniaxially stretching and releasing between 0 and 60% at a strain rate of 0.013/s. The vertical compression tests involved compression up to 40% applied by carefully sandwiching the device between two stiff plates and displacing the top plate using a piezoelectric stage (PI-USA, Waltham, MA). The total compression was estimated on the basis of the initial nominal coil diameter of 660 μm. Applying force through a steel spherical probe to the cover glass base (see fig. S7) ensured that the sandwiching plates remained in a parallel configuration. In addition, force measurements and side-view monitoring confirmed the uniform loading on multiple coils. Force was measured through the displacement of a 4-bar flexure monitored by capacitive sensors (Lion Precision, Oakdale, MN). The transducer stiffness was ≈ 1020 N/m, much stiffer than the out-of-plane stiffness of the devices themselves; the flexure displacement was added to the prescribed displacement for vertical compression to reach targeted values.

SUPPLEMENTARY MATERIALS

Supplementary material for this article is available at http://advances.sciencemag.org/cgi/content/full/4/11/eaau5849/DC1

Note S1. Step-by-step fabrication procedures for 3D compliant and stretchable thermoelectric coils.
Note S2. Power optimization in thermoelectric harvesters.
Note S3. Effect of PI width on the pop-up yield for 3D coils.
Note S4. Mechanical compression test.
Fig. S1. Schematic step-by-step fabrication procedures for 3D compliant and stretchable thermoelectric coils.
Fig. S2. Design of the 2D precursor for the 8 × 8 array.
Fig. S3. Illustration of geometric parameters.
Fig. S4. Mechanics of the in-plane stretching process for the 3D spring coil.
Fig. S5. Polyimide width effect on yield of buckle-up process.
Fig. S6. Simulated strain/stress distribution in the encapsulation and metal layers.
Fig. S7. Mechanical compression testing.
Fig. S8. Mechanics of the vertical compression process of the 3D spring coil.
Fig. S9. Schematic illustration of the testing setup for measuring the thermoelectric response of the devices.
Fig. S10. Thermoelectric properties for heavily doped n-type and p-type silicon thin films measured in the silicon-on-insulator wafer form before patterning.
Fig. S11. Output characteristics of the 3 × 1 harvester shown in Fig. 1B.
Fig. S12. Preliminary thermal modeling by replacing silicon with other thermoelectric materials.
Fig. S13. The design that uses multilayer stacking to improve the power density.

REFERENCES AND NOTES

1. G. J. Snyder, in *Energy Harvesting Technologies*, S. Priya, D. J. Inman, Eds. (Springer US, 2009), pp. 325–336.
2. S. J. Kim, J. H. We, B. J. Cho, A wearable thermoelectric generator fabricated on a glass fabric. *Energ. Environ. Sci.* **7**, 1959–1965 (2014).
3. J.-H. Bahk, H. Fang, K. Yazawa, A. Shakouri, Flexible thermoelectric materials and device optimization for wearable energy harvesting. *J. Mater. Chem. C* **3**, 10362–10374 (2015).
4. D. Beretta, A. Perego, G. Lanzani, M. Caironi, Organic flexible thermoelectric generators: From modeling, a roadmap towards applications. *Sustainable Energy Fuels* **1**, 174–190 (2017).
5. S. Priya, D. J. Inman, *Energy Harvesting Technologies* (Springer US, 2009).
6. C. Dagdeviren, Z. Li, Z. L. Wang, Energy harvesting from the animal/human body for self-powered electronics. *Annu. Rev. Biomed. Eng.* **19**, 85–108 (2017).
7. J. Peng, S. D. Kang, G. J. Snyder, Optimization principles and the figure of merit for triboelectric generators. *Sci. Adv.* **3**, eaap8576 (2017).
8. W. Lim, I. Lee, D. Sylvester, D. Blaauw, Batteryless Sub-nW Cortex-M0+ processor with dynamic leakage-suppression logic, in *2015 IEEE International Solid-State Circuits Conference*, San Francisco, CA, USA, 22 to 26 February 2015 (IEEE, 2015), pp. 1–3.
9. P. P. Mercier, S. Bandyopadhyay, A. C. Lysaght, K. M. Stankovic, A. P. Chandrakasan, A sub-nW 2.4 GHz transmitter for low data-rate sensing applications. *IEEE J. Solid-State Circuits* **49**, 1463–1474 (2014).
10. P. P. Mercier, A. C. Lysaght, S. Bandyopadhyay, A. P. Chandrakasan, K. M. Stankovic, Energy extraction from the biologic battery in the inner ear. *Nat. Biotechnol.* **30**, 1240–1243 (2012).
11. P. Nadeau, M. Mimee, S. Carim, T. K. Lu, A. P. Chandrakasan, Nanowatt circuit interface to whole-cell bacterial sensors, in *2017 IEEE International Solid-State Circuits Conference*, San Francisco, CA, USA, 5 to 9 February 2017 (IEEE, 2017), pp. 352–353.
12. T. Varghese, C. Hollar, J. Richardson, N. Kempf, C. Han, P. Gamarachchi, D. Estrada, R. J. Mehta, Y. Zhang, High-performance and flexible thermoelectric films by screen printing solution-processed nanoplate crystals. *Sci. Rep.* **6**, 33135 (2016).
13. J. Choi, K. Cho, S. Kim, Flexible thermoelectric generators composed of n- and p-type silicon nanowires fabricated by top-down method. *Adv. Energy Mater.* **7**, 1602138 (2017).
14. J. P. Rojas, D. Conchouso, A. Arevalo, D. Singh, I. G. Foulds, M. M. Hussain, Paper-based origami flexible and foldable thermoelectric nanogenerator. *Nano Energy* **31**, 296–301 (2017).
15. G. J. Snyder, J. R. Lim, C.-K. Huang, J.-P. Fleurial, Thermoelectric microdevice fabricated by a MEMS-like electrochemical process. *Nat. Mater.* **2**, 528–531 (2003).
16. U. Pelz, J. Jaklin, R. Rostek, F. Thoma, M. Kröner, P. Woias, Fabrication process for micro thermoelectric generators (μTEGs). *J. Electron. Mater.* **45**, 1502–1507 (2016).
17. S. Shin, R. Kumar, J. W. Roh, D.-S. Ko, H.-S. Kim, S. Il Kim, L. Yin, S. M. Schlossberg, S. Cui, J.-M. You, S. Kwon, J. Zheng, J. Wang, R. Chen, High-performance screen-printed thermoelectric films on fabrics. *Sci. Rep.* **7**, 7317 (2017).
18. M. Kishi, H. Nemoto, T. Hamao, M. Yamamoto, S. Sudou, M. Mandai, S. Yamamoto, Micro thermoelectric modules and their application to wristwatches as an energy source, in *1999 Eighteenth International Conference on Thermoelectrics*, Baltimore, Maryland, USA, 29 August to 2 September 1999 (IEEE, 1999), pp. 301–307.
19. J. Weber, K. Potje-Kamloth, F. Haase, P. Detemple, F. Völklein, T. Doll, Coin-size coiled-up polymer foil thermoelectric power generator for wearable electronics. *Sens. Actuators A Phys.* **132**, 325–330 (2006).

20. F. Suarez, D. P. Parekh, C. Ladd, D. Vashaee, M. D. Dickey, M. C. Öztürk, Flexible thermoelectric generator using bulk legs and liquid metal interconnects for wearable electronics. *Appl. Energy* **202**, 736–745 (2017).
21. C. Wan, X. Gu, F. Dang, T. Itoh, Y. Wang, H. Sasaki, M. Kondo, K. Koga, K. Yabuki, G. J. Snyder, R. Yang, K. Koumoto, Flexible n-type thermoelectric materials by organic intercalation of layered transition metal dichalcogenide TiS_2. *Nat. Mater.* **14**, 622–627 (2015).
22. C. Wan, R. Tian, A. B. Azizi, Y. Huang, Q. Wei, R. Sasai, S. Wasusate, T. Ishida, K. Koumoto, Flexible thermoelectric foil for wearable energy harvesting. *Nano Energy* **30**, 840–845 (2016).
23. Y. Sun, L. Qiu, L. Tang, H. Geng, H. Wang, F. Zhang, D. Huang, W. Xu, P. Yue, Y. S. Guan, F. Jiao, Y. Sun, D. Tang, C. A. Di, Y. Yi, D. Zhu, Flexible n-type high-performance thermoelectric thin films of poly(nickel-ethylenetetrathiolate) prepared by an electrochemical method. *Adv. Mater.* **28**, 3351–3358 (2016).
24. B. Russ, A. Glaudell, J. J. Urban, M. L. Chabinyc, R. A. Segalman, Organic thermoelectric materials for energy harvesting and temperature control. *Nat. Rev. Mater.* **1**, 16050 (2016).
25. S. D. Kang, G. J. Snyder, Charge-transport model for conducting polymers. *Nat. Mater.* **16**, 252–257 (2017).
26. C.-K. Mai, B. Russ, S. L. Fronk, N. Hu, M. B. Chan-Park, J. J. Urban, R. A. Segalman, M. L. Chabinyc, G. C. Bazan, Varying the ionic functionalities of conjugated polyelectrolytes leads to both p- and n-type carbon nanotube composites for flexible thermoelectrics. *Energ. Environ. Sci.* **8**, 2341–2346 (2015).
27. C. Cho, K. L. Wallace, P. Tzeng, J.-H. Hsu, C. Yu, J. C. Grunlan, Outstanding low temperature thermoelectric power factor from completely organic thin films enabled by multidimensional conjugated nanomaterials. *Adv. Energy Mater.* **6**, 1502168 (2016).
28. A. D. Avery, K. S. Mistry, S. L. Guillot, B. L. Zink, Y.-H. Kim, J. L. Blackburn, A. J. Ferguson, Tailored semiconducting carbon nanotube networks with enhanced thermoelectric properties. *Nat. Energy* **1**, 16033 (2016).
29. B. A. MacLeod, N. J. Stanton, I. E. Gould, D. Wesenberg, R. Ihly, Z. R. Owczarczyk, K. E. Hurst, C. S. Fewox, C. N. Folmar, K. Holman Hughes, B. L. Zink, J. L. Blackburn, A. J. Ferguson, Large n- and p-type thermoelectric power factors from doped semiconducting single-walled carbon nanotube thin films. *Energ. Environ. Sci.* **10**, 2168–2179 (2017).
30. O. Bubnova, Z. Ullah Khan, A. Malti, S. Braun, M. Fahlman, M. Berggren, X. Crispin, Optimization of the thermoelectric figure of merit in the conducting polymer poly(3,4-ethylenedioxythiophene). *Nat. Mater.* **10**, 429–433 (2011).
31. S. Xu, Z. Yan, K.-I. Jang, W. Huang, H. Fu, J. Kim, Z. Wei, M. Flavin, J. McCracken, R. Wang, A. Badea, Y. Liu, D. Xiao, G. Zhou, J. Lee, H. U. Chung, H. Cheng, W. Ren, A. Banks, X. Li, U. Paik, R. G. Nuzzo, Y. Huang, Y. Zhang, J. A. Rogers, Assembly of micro/nanomaterials into complex, three-dimensional architectures by compressive buckling. *Science* **347**, 154–159 (2015).
32. Z. Yan, M. Han, Y. Shi, A. Badea, Y. Yang, A. Kulkarni, E. Hanson, M. E. Kandel, X. Wen, F. Zhang, Y. Luo, Q. Lin, H. Zhang, X. Guo, Y. Huang, K. Nan, S. Jia, A. W. Oraham, M. B. Mevis, J. Lim, X. Guo, M. Gao, W. Ryu, K. Jun Yu, B. G. Nicolau, A. Petronico, S. S. Rubakhin, J. Lou, P. M. Ajayan, K. Thornton, G. Popescu, D. Fang, J. V. Sweedler, P. V. Braun, H. Zhang, R. G. Nuzzo, Y. Huang, Y. Zhang, J. A. Rogers, Three-dimensional mesostructures as high-temperature growth templates, electronic cellular scaffolds, and self-propelled microrobots. *Proc. Natl. Acad. Sci. U.S.A.* **114**, E9455–E9464 (2017).
33. K.-I. Jang, K. Li, H. Uk Chung, S. Xu, H. Na Jung, Y. Yang, J. Won Kwak, H. Hee Jung, J. Song, C. Yang, A. Wang, Z. Liu, J. Yoon Lee, B. Hoon Kim, J.-H. Kim, J. Lee, Y. Yu, B. Jun Kim, H. Jang, K. Jun Yu, J. Kim, J. Woo Lee, J.-W. Jeong, Y. Min Song, Y. Huang, Y. Zhang, J. A. Rogers, Self-assembled three dimensional network designs for soft electronics. *Nat. Commun.* **8**, 15894 (2017).
34. Y. Zhang, F. Zhang, Z. Yan, Q. Ma, X. Li, Y. Huang, J. A. Rogers, Printing, folding and assembly methods for forming 3D mesostructures in advanced materials. *Nat. Rev. Mater.* **2**, 17019 (2017).
35. H. Fu, K. Nan, W. Bai, W. Huang, K. Bai, L. Lu, C. Zhou, Y. Liu, F. Liu, J. Wang, M. Han, Z. Yan, H. Luan, Y. Zhang, Y. Zhang, J. Zhao, X. Cheng, M. Li, J. Woo Lee, Y. Liu, D. Fang, X. Li, Y. Huang, Y. Zhang, J. A. Rogers, Morphable 3D mesostructures and microelectronic devices by multistable buckling mechanics. *Nat. Mater.* **17**, 268–276 (2018).
36. J. Vedde, P. Gravesen, The fracture strength of nitrogen doped silicon wafers. *Mater. Sci. Eng. B* **36**, 246–250 (1996).
37. L. L. Baranowski, G. J. Snyder, E. S. Toberer, Effective thermal conductivity in thermoelectric materials. *J. Appl. Phys.* **113**, 204904 (2013).
38. Z. Wang, V. Leonov, P. Fiorini, C. V. Hoof, Realization of a wearable miniaturized thermoelectric generator for human body applications. *Sens. Actuators A Phys.* **156**, 95–102 (2009).
39. S. S. Kim, S. Yamamoto, T. Aizawa, Thermoelectric properties of anisotropy-controlled p-type Bi–Te–Sb system via bulk mechanical alloying and shear extrusion. *J. Alloys Compd.* **375**, 107–113 (2004).
40. K. Ueno, A. Yamamoto, T. Noguchi, T. Inoue, S. Sodeoka, H. Obara, Optimization of hot-press conditions of Zn_4Sb_3 for high thermoelectric performance. II. Mechanical properties. *J. Alloys Compd.* **388**, 118–121 (2005).
41. K. Tyagi, B. Gahtori, S. Bathula, M. Jayasimhadri, S. Sharma, N. K. Singh, D. Haranath, A. K. Srivastava, A. Dhar, Crystal structure and mechanical properties of spark plasma sintered Cu_2Se: An efficient photovoltaic and thermoelectric material. *Solid State Commun.* **207**, 21–25 (2015).
42. Z. Yan, F. Zhang, F. Liu, M. Han, D. Ou, Y. Liu, Q. Lin, X. Guo, H. Fu, Z. Xie, M. Gao, Y. Huang, J. H. Kim, Y. Qiu, K. Nan, J. Kim, P. Gutruf, H. Luo, A. Zhao, K.-C. Hwang, Y. Huang, Y. Zhang, J. A. Rogers, Mechanical assembly of complex, 3D mesostructures from releasable multilayers of advanced materials. *Sci. Adv.* **2**, e1601014 (2016).
43. S. Iwanaga, G. J. Snyder, Scanning Seebeck coefficient measurement system for homogeneity characterization of bulk and thin-film thermoelectric materials. *J. Electron. Mater.* **41**, 1667–1674 (2012).
44. T. Caillat, J.-P. Fleurial, A. Borshchevsky, Preparation and thermoelectric properties of semiconducting Zn_4Sb_3. *J. Phys. Chem. Solid* **58**, 1119–1125 (1997).
45. T. Kanno, H. Tamaki, H. K. Sato, S. D. Kang, S. Ohno, K. Imasato, J. J. Kuo, G. J. Snyder, Y. Miyazaki, Enhancement of average thermoelectric figure of merit by increasing the grain-size of $Mg_{3.2}Sb_{1.5}Bi_{0.49}Te_{0.01}$. *Appl. Phys. Lett.* **112**, 033903 (2018).
46. S. D. Kang, S. A. Danilkin, U. Aydemir, M. Avdeev, A. Studer, G. J. Snyder, Apparent critical phenomena in the superionic phase transition of $Cu_{2-x}Se$. *New J. Phys.* **18**, 013024 (2016).
47. M. Ferhat, J. Nagao, Thermoelectric and transport properties of β-Ag_2Se compounds. *J. Appl. Phys.* **88**, 813–816 (2000).
48. J. A. Perez-Taborda, O. Caballero-Calero, L. Vera-Londono, F. Briones, M. Martin-Gonzalez, High thermoelectric *zT* in n-type silver selenide films at room temperature. *Adv. Energy Mater.* **8**, 1702024 (2018).
49. S. I. Kim, K. H. Lee, H. A. Mun, H. S. Kim, S. W. Hwang, J. W. Roh, D. J. Yang, W. H. Shin, X. S. Li, Y. H. Lee, G. J. Snyder, S. W. Kim, Dense dislocation arrays embedded in grain boundaries for high-performance bulk thermoelectrics. *Science* **348**, 109–114 (2015).
50. H.-S. Kim, N. A. Heinz, Z. M. Gibbs, Y. Tang, S. D. Kang, G. Jeffrey Snyder, High thermoelectric performance in $(Bi_{0.25}Sb_{0.75})_2Te_3$ due to band convergence and improved by carrier concentration control. *Mater. Today* **20**, 452–459 (2017).

Acknowledgments: We thank X. Shan for the help in taking and processing images. **Funding:** We acknowledge the support from the U.S. Department of Energy, Office of Science, Basic Energy Sciences through the following programs: J.A.R. acknowledges DE-FG02-07ER46471; G.J.S. acknowledges S3TEC, an Energy Frontier Research Center (DE-SC0001299). Y.H. acknowledges the support from the NSF (1400169, 1534120, and 1635443). Z.X. acknowledges the support from the National Natural Science Foundation of China (11402134). K.J.Y. acknowledges the support from the National Research Foundation of Korea (NRF-2017M1A2A2048880 and NRF-2018M3A7B4071109) and the Yonsei University Future-leading Research Initiative (RMS2 2018-22-0028). The experimental work was carried out, in part, in the Frederick Seitz Materials Research Laboratory, Central Research Facilities, University of Illinois. **Author contributions:** K.N. developed the fabrication process and produced the device. S.D.K. oversaw the thermal and thermoelectric analyses, measured the thermoelectric properties, and modeled the thermal and power characteristics. K.L. designed the 3D coil structure, optimized the geometric parameters based on coupled thermal and mechanical FEA, and drew the masks. A.C.D. did the mechanical characterization. K.J.Y., J.W., and C.Z. assisted the fabrication process. F.Z., Z.X., and H.W. assisted the FEA and optimization. M.T.A. assisted thermoelectric characterization. H.L. helped to design the mask. S.D.K., K.N., and K.L. wrote the manuscript. Y.Z., Y.H., G.J.S., and J.A.R. supervised the project. All authors reviewed or edited the manuscript. **Competing interests:** The authors declare that they have no competing interests. **Data and materials availability:** All data needed to evaluate the conclusions in the paper are present in the paper and/or the Supplementary Materials. Additional data related to this paper may be requested from the authors.

Submitted 26 June 2018
Accepted 2 October 2018
Published 2 November 2018
10.1126/sciadv.aau5849

Citation: K. Nan, S. D. Kang, K. Li, K. J. Yu, F. Zhu, J. Wang, A. C. Dunn, C. Zhou, Z. Xie, M. T. Agne, H. Wang, H. Luan, Y. Zhang, Y. Huang, G. J. Snyder, J. A. Rogers, Compliant and stretchable thermoelectric coils for energy harvesting in miniature flexible devices. *Sci. Adv.* **4**, eaau5849 (2018).